The Electro-Thermal Properties of Integrated Circuit Microbolometers

Speaker / Author: M. du Plessis*
Co-author(s): J. Schoeman*, W. Maclean* and C. Schutte**

*Carl and Emily Fuchs Institute for Microelectronics, University of Pretoria
Lynnwood Road, Pretoria, 0002, South Africa
e-mail: monuko@up.ac.za
Phone: 012 420 2952 Fax: 012 362 5115

**Denel Aerospace Systems (Detek)
P.O. Box 7412, Centurion, 0046, South Africa

Abstract

The use of uncooled infrared sensors in thermal imaging is a fast growing market in the fields of security and health. The integration of uncooled or room temperature infrared sensors onto a silicon CMOS chip will facilitate the manufacture of large imaging arrays. At the University of Pretoria we are researching the integration of microbolometer infrared sensors onto CMOS readout electronic circuits using post processing techniques. The microbolometer utilises the change in resistance of a temperature sensitive resistive material, e.g. vanadium oxide or a thin metal film, to measure the amount of infrared radiation falling onto the device and heating the device. The microbolometer structure should be thermally isolated from the bulk silicon to achieve the required sensitivity.

In this paper we will describe the device structures, as well as the techniques we used to determine experimentally the electrical, thermal and electro-thermal properties of the devices. Of interest to us are the following parameters: 1) temperature coefficient of the bolometer resistive layer, 2) thermal conductivity of the device, 3) thermal capacitance of the total sensor structure and 4) the thermal time constant. The microbolometer thermal characteristics can also be modelled and simulated using CoventorWare software.

1. Introduction

The two principal types of infrared (IR) detectors are 1) photon detectors, and 2) thermal detectors [1]. In photon detectors the absorbed photons produce free electrons and holes in the semiconductor material, to generate a photon-induced current or voltage, either in a photoconductive or photovoltaic mode. Photon detectors have high signal to noise ratios, sensitivity and very fast response, but requires cryogenic cooling systems, which are bulky and expensive In thermal detectors the absorbed photons produce a temperature change, which can then indirectly be detected by measuring a temperature dependent property of the detector material.

Uncooled thermal detectors provide much lower cost, are more compact and dissipate less power. Uncooled IR sensors have been developed in recent years for both military and civilian applications like night vision cameras for surveillance and digital infrared thermal imaging for health applications. Recent advances in micromachining technology allow the fabrication of sensitive thermal detectors that can operate at room temperature and be easily integrated with CMOS readout electronics. This leads to a decrease in power consumption and system cost, which makes hand-held infrared cameras possible.

Thermal sensors can be used in two ways [2], namely as 1) direct sensors which convert thermal signals (temperature or heat) into electrical signals, or 2) indirect sensors which are based on thermal actuation effects, for example thermo-mechanical (thermal expansion, bimorph) effects. In this paper we will only consider direct sensors, since it is the most mature technology.

Direct thermal detectors are based on three common approaches [3], namely 1) bolometers, 2) pyroelectric effects, and 3) thermoelectric effects. A bolometer changes its resistance according to the change of the temperature, and thus a high temperature coefficient of resistance (TCR) is needed for high sensitivity. The pyroelectric effect is exhibited by ferroelectric crystals that exhibit electric polarization. The thermoelectric effect takes place when two junctions made of two different materials are at different temperatures, and the magnitude of the voltage generated across the junction (thermopile) depends on the materials and the temperature difference between the junctions. The bolometer type of detector exhibits a much higher responsivity than that of thermopiles, and it is also easier to fabricate than pyroelectric detectors.

The bolometer technology is commercially available in large imaging arrays. In figure 1 a schematic of the bolometer principle is shown, as well as the conventional thermal model.

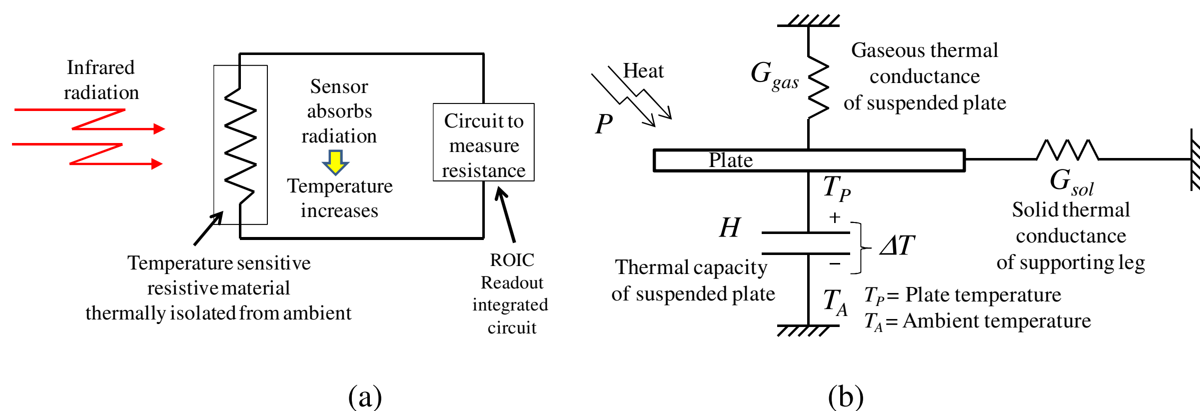

Figure 1. (a) Principle of thermal bolometer sensor, and (b) equivalent thermal schematic.

Infrared radiation falls onto the bolometer device, as shown in figure 1. The radiation is absorbed by the bolometer device, and if the bolometer is relatively well thermally isolated from the ambient, the temperature of the bolometer will increase. If the bolometer material has a high temperature coefficient of resistance (TCR), the read out circuit can measure the change in resistance and the resistance change will be an indication of the amount of infrared radiation falling onto the bolometer. It is obvious that to achieve a large sensitivity, the bolometer should have a high IR absorption factor, a large TCR and low thermal conductance to the ambient.

2. Conventional approach to device thermal properties

The analysis of all types of IR sensors begins with a heat flow equation that describes the temperature rise in terms of absorbed radiant power. There are two potential mechanisms of heat transfer [1], namely 1) thermal conduction, and 2) thermal radiation. Thermal conduction occurs in two ways. Heat flows from the sensor along its mechanical support to

the substrate, and heat also flows through the surrounding atmosphere. In practice, the thermal radiation is so small that it can be ignored.

Referring to figure 1, the rise in temperature ΔT of the bolometer plate is given by [1]

$$\Delta T = \frac{\eta P_O}{G\sqrt{1+4\pi^2 f^2 \tau^2}} \qquad ^\circ C$$

with
η = fraction of IR power absorbed
P_O = incident infrared power on detector, W
G = total thermal conductance to substrate, W/K
f = frequency of modulation of radiation, Hz
τ = thermal time constant = H/G, sec
H = thermal capacitance, J/K

If the bolometer is biased with a constant bias current I_B, the voltage responsivity R_V of the bolometer detector is given by

$$R_V = I_B \times R_B \times \alpha \times \Delta T \quad V/W$$

with
I_B = bolometer bias current, A
R_B = bolometer resistance, Ω

$$\alpha = TCR = \frac{1}{R_B}\frac{dR_B}{dT} = \frac{d(\ln R_B)}{dT}, \quad \%/K$$

From the above it can be seen that the bolometer voltage signal responsivity R_V is directly proportional to the infrared absorption coefficient η and the bolometer temperature coefficient TCR, and inversely proportional to the thermal conductance G. It is therefore important that the mechanical design of the bolometer support structure must be optimized to minimize thermal conductance G.

Noise will also be generated within the bolometer imaging system. The noise equivalent temperature difference (NETD in K) is the most important figure of merit used to describe a complete IR imaging system, including the imaging optics. It is defined as the temperature difference on a black object that produces a signal to noise ratio of one at the system output.

$$NETD \propto \frac{v_n G}{A_d \eta \alpha}$$

with v_n the noise voltage and A_d the detector area.

The above equation for NETD also shows the relationship between detector area A_d and thermal conductance G to achieve good performance (small NETD). By scaling down to smaller pixel sizes to facilitate the manufacture of larger imaging arrays, the thermal conductance should scale down with detector area. This is difficult, since the length of the connecting legs connecting the thermally isolated microbolometer membrane to the bulk material will determine the thermal conductance in vacuum, needing long legs to achieve a small thermal conductance. The connecting legs can also not take up to much of the pixel area, since the effective fill factor will be reduced.

Knowledge of the thermal properties of the microbolometer membrane is crucial for obtaining optimal performance of the thermal IR detector. The thermal parameter estimations using the conventional approach are discussed below, using figure 1(b) as reference,

The thermal conductance G of a detector is dominated by the sum of two components [4]:

$$G = G_{gas} + G_{sol}$$

G_{gas} is the conductance through the surrounding gas from plate to substrate and G_{sol} is the conductance through the solid material of the legs supporting the plate.

$$G_{gas} = \lambda_{gas} \frac{A_d}{d_s}$$

where

A_d = device area, m^2

d_s = plate to substrate separation, m

λ_{gas} = gas thermal conductivity = 0.026 W/mK for nitrogen at 300K and 1 atm pressure
= 0 in vacuum

$G_{sol} = 2 \times G_{leg}$ when two legs support the plate (see figure 3), with G_{leg} the thermal conductance of one leg. The supporting legs may consist of several layers of different materials. In this case the conductances can be added as a result of parallel conducting paths, and the total leg conductance G_{leg} for one leg will be given by

$$G_{leg} = \sum_i \lambda_i \frac{W_i d_i}{l_i}$$

where

W_i = width of supporting leg

d_i = thickness of supporting leg

l_i = length of supporting leg

λ_i = thermal conductivity of supporting leg material

It has recently been proposed [5] that the multilayer supporting leg (and suspended plate) can be expressed in terms of an equivalent solid thermal conductivity G_e, with

$$G_e = \lambda_e \frac{W_e d_e}{L_e} = \sum_i \lambda_i \frac{W_i d_i}{l_i}$$

where

W_e = width of supporting leg

d_e = total thickness of supporting leg

L_e = length of supporting leg

λ_e = equivalent thermal conductivity of supporting leg

and

$$\lambda_e = \frac{1}{W_e d_e} \sum_i \lambda_i W_i d_i$$

The multilayer supporting leg structure of the bolometer can now be represented as a single homogenous structure. The same can be done for the suspended plate region.

Under vacuum conditions, the leg conductance will be the dominant thermal conductance, while under atmospheric pressure conditions the gaseous heat transfer will dominate.

In general the heat capacity H is given by

$$H = V \rho c \qquad J/K$$

with

V = volume of the detector plate, cm^3

ρ = the density of the plate material, g/cm^3

c = the specific heat of the plate material, J/gK

Also, the heat capacity H must be chosen to meet the thermal time constant τ requirement, with

$$\tau = \frac{H}{G} \qquad \text{sec}$$

Normally two dimensional staring arrays are used in bolometer imaging applications. A good choice is to make the pixel time response (equal to the bolometer thermal time constant τ) approximately a third of the frame time (= 1/frame rate). This usually means a thermal time constant τ in the range of 10 ms is required.

3. Device structure

Thermal sensors based on CMOS technology became feasible when CMOS micromachining was established. Micromachining makes it possible to remove thermally conducting material for the thermal isolation of heated microstructures. While thermal effects are intuitively considered to be slow, the small size of CMOS microsensors brings about time constants in the millisecond range. Thermally based sensors can be made by combining the well-established industrial CMOS technology with additional compatible processing steps. In our case, the additional compatible processing steps (deposition, lithography and etching) was performed as post-processing, where the additional steps are performed after the completion of the regular IC process sequence.

A typical device we designed and manufactured using one of the CMOS aluminium layers as sacrificial layer, is shown in figure 2. The bolometer thin film resistance layer was a 60 nm thick and 5 μm wide Ti layer sandwiched in an oxide-nitride membrane structure. The cavity dimension was designed to be 2 micron. The two layout dimensions to be investigated are shown in the photomicrograph of figure 3, just after the membrane definition photolithographic step and before the aluminium sacrificial layer etching during manufacture. Device FA1 has a larger membrane area, but also longer connecting legs than device FA2. One would expect FA1 to have the higher thermal conductance at atmospheric pressure because of the larger membrane area, but FA1 should at the same time have the lower thermal conductance under vacuum conditions due to the longer connecting legs, compared to device FA2.

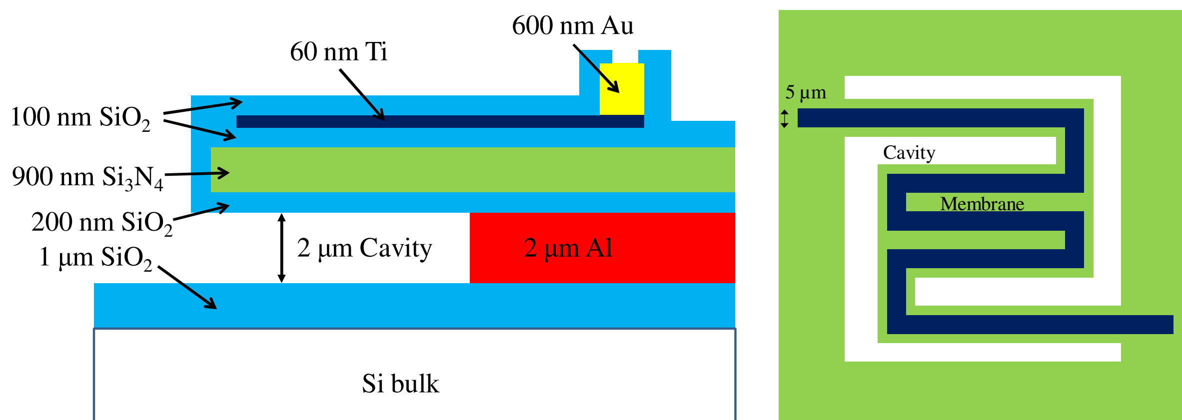

Figure 2. Microbolometer structure and layout

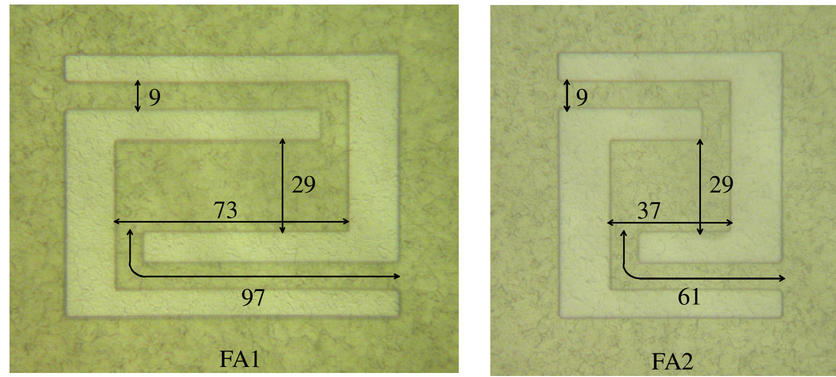

Figure 3. Photomicrographs of two microbolometer membranes with dimensions in micron.

4. Modified device thermal modelling

In this paper we present a modified approach to the analytical description of metal thin film bolometer thermal properties. The conventional approach described in section 2 and in figure 1(b) is widely used for all types of bolometers, although it is better suited for devices where the power is dissipated only on the suspended plate, like in the case of high resistance vanadium oxide bolometers, and not within the supporting legs as well. In metal film bolometers power is being dissipated uniformly along the length of the resistor on both the suspended plate and supporting legs.

Four modifications are proposed, namely 1) the effect of sidewall gaseous conduction, 2) a characteristic thermal length constant L_{th}, 3) a distributed thermal resistance network in the bolometer, and 4) a constriction thermal resistance R_C where the supporting leg connects to the suspended the plate.

The first modification is to include the sidewall heat conduction in the atmospheric analysis. The gaseous thermal conduction is illustrated in figure 4. As the supporting leg and plate dimensions are shrunk, the sidewall effect will become more pronounced. The sidewall conduction will have the effect of increasing the effective area A_d used in the calculation of the gaseous thermal conductance.

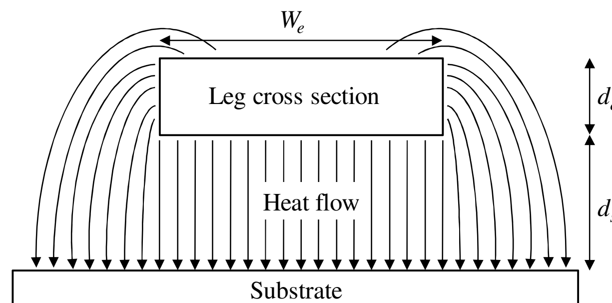

Figure 4. Distributed thermal resistance model for atmospheric pressure condition.

In our model the effect of the sidewall conduction will be to add a conductance in parallel to the conventional vertical heat flow. Assuming an effective conducting distance d_s+d_e from the sidewall to the substrate, in case of the supporting legs the effective area $A_d = W_eL_e$ will be increased by a factor F_{swl}, with

$$F_{swl} = 1 + \frac{d_s}{W_e} \frac{2d_e}{d_s + d_e} = 1.18$$

The above value of factor F_{swl} will be the same for both devices FA1 and FA2.

In the case of the suspended plate with dimensions $W_p \times L_p$, the effective area will be increased by the factor F_{swp}, with

$$F_{swp} = 1 + \frac{d_s}{W_p L_p} \frac{2(W_p + L_p - W_e)d_e}{d_s + d_e}$$

The plate factor F_{swp} =1.10 for device FA1 and factor F_{swp} =1.13 for device FA2.

The effect of a characteristic thermal length constant is illustrated in figure 5. In this figure is shown heat flow P entering one side of the supporting leg, and the resultant variation in temperature $T(x)$ along the leg. The per unit length thermal resistance and conductance in the distributed model are r_{sol} and g_{gas}.

$$r_{sol} = \frac{1}{\lambda_e W_e d_e} \quad , \quad g_{gas} = \frac{\lambda_{gas} W_e}{d_s}$$

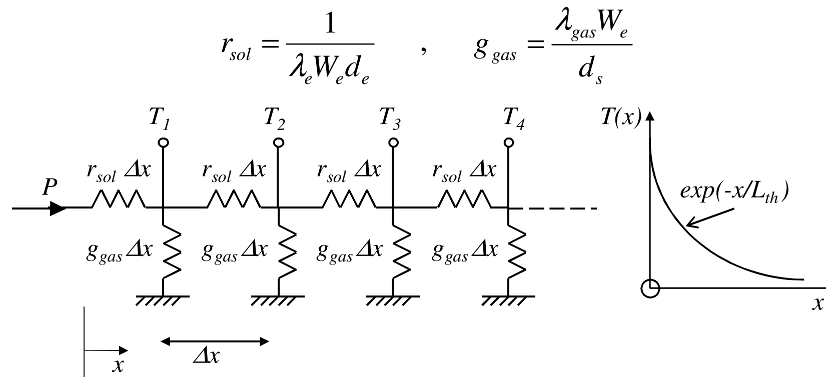

Figure 5. Distributed thermal resistance model for atmospheric pressure condition.

The temperature $T(x)$ at any position x is simply the temperature $T(0)$ times an exponential factor.

$$T(x) = T(0)\, e^{-x/L_{th}}$$

with characteristic length

$$L_{th} = \sqrt{\frac{1}{r_{sol} g_{gas}}} = \sqrt{\frac{\lambda_e}{\lambda_{gas}} d_e d_s}$$

The next case to be viewed is the situation in vacuum where heat is generated along the length of a bolometer section. This is illustrated in figure 6.

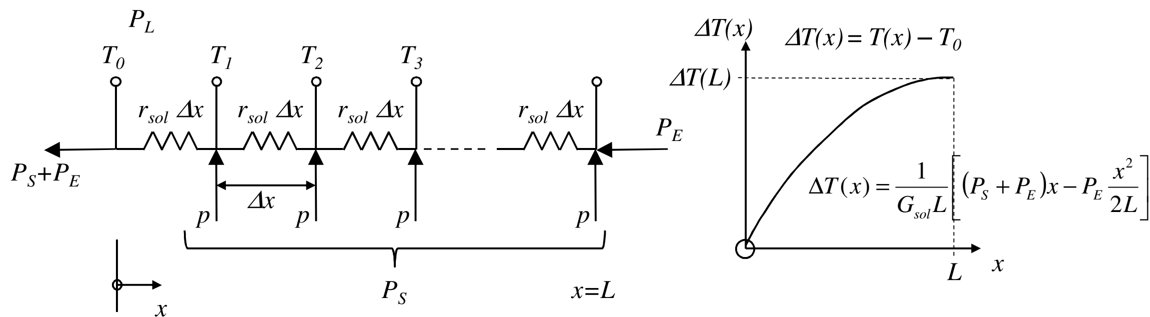

Figure 6. Distributed thermal resistance model for vacuum condition.

In figure 6 is shown the length L of the section, with heat flow p into each section of length Δx. At the end of the section heat P_E flows into the section from an adjacent section. From figure 6 the parabolic expression for temperature variation $\Delta T(x)$ can be derived.

$$\Delta T(x) = \frac{1}{G_{sol}L}\left[(P_S + P_E)x - P_S\frac{x^2}{2L}\right] \quad \text{and} \quad \Delta T(L) = \frac{1}{G_{sol}}\left(P_E + \frac{P_S}{2}\right)$$

where G_{sol} = total thermal conductance = $1/(L\times r_{sol})$, P_S = total heat flow into section = Σp.

Since the microbolometer legs are much narrower than the plate, radial heat conduction is constricted as the heat flows from a wider to narrower cross-section. The analytical model [6] uses a constriction thermal resistance R_C, which accounts for the heat flowing from a wider to a narrower cross-section. The constriction resistance R_C is given by [6]

$$R_C = \frac{1}{\pi d_e \lambda_e}\left[\left(\varepsilon + \frac{1}{\varepsilon}\right)\ln\frac{1+\varepsilon}{1-\varepsilon} + 2\ln\frac{1-\varepsilon^2}{4\varepsilon}\right]$$

with $\varepsilon = \dfrac{W_e}{W_p}$ and W_p = width of plate.

In our approximation the constriction resistance will be distributed over the characteristic length L_{th} into both the plate and the supporting leg.

5. Analytical modelling and CoventorWare simulation

The thermal properties of the two test devices were calculated from the device dimensions in figures 2 and 3, analytical expressions of section 2 and 4, and the thermal parameters listed in table 1.

Table 1. Thermal constants used in prototype calculations

Material	**Thermal conductivity λ W/mK**	**Specific heat c J/gK**	**Density g/cm^3**
CVD Silicon dioxide	0.76	1	2.22
CVD Silicon nitride	1.65	1.2	3.10
Titanium	16.3	0.5	4.51

The parameters used in the analytical model are given in table 2.

Table 2. Thermal parameters used in prototype calculations

Test device	**Width W_e µm**	**Thickness d_e µm**	**Conductivity λ_e W/mK**	**Length L_{th} µm**	**Width W_p µm**	**Resistance R_C mK/W**
FA1	9	1.36	1.71	13.4	73	469×10^3
FA2	9	1.36	1.71	13.4	37	287×10^3

Using the above values and analytical expressions, the temperature profiles in the test devices could be estimated. The test devices were also simulated using CoventorWare software.

In figure 7(a) is shown the two dimensional CoventorWare temperature profile in the FA1 device, and in figure 7(b) is shown the one dimensional temperature profile along the supporting leg from the substrate to the centre of the plate, under atmospheric pressure conditions. The three temperature profiles are: 1) the conventional analysis, 2) the modified analysis, and 3) the CoventorWare simulated results.

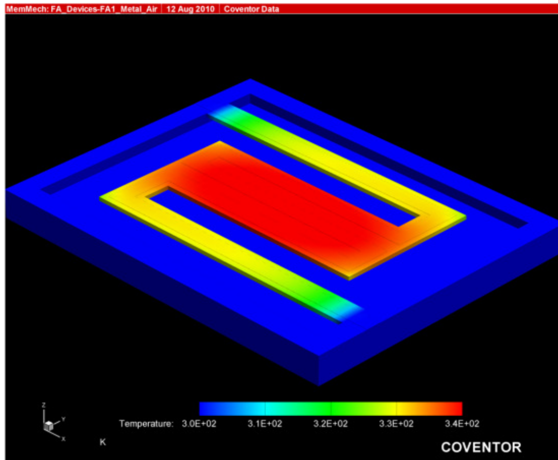

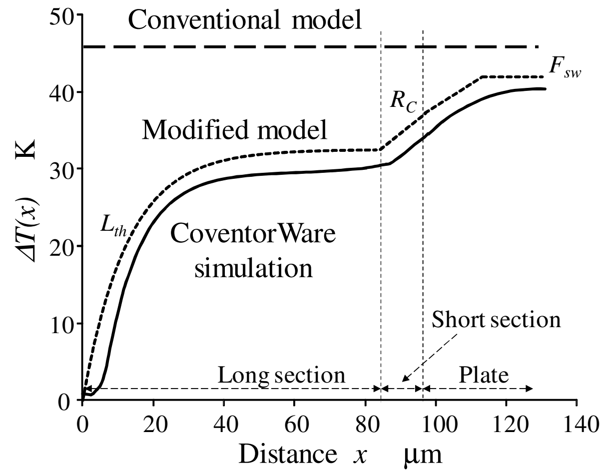

(a) (b)

Figure 7. (a) CoventorWare 3-D thermal profile, and (b) CoventorWare and analytical 2-D thermal profiles at atmospheric pressure for device FA1.

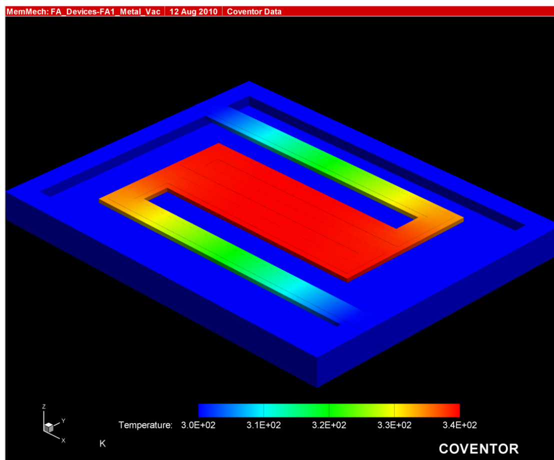

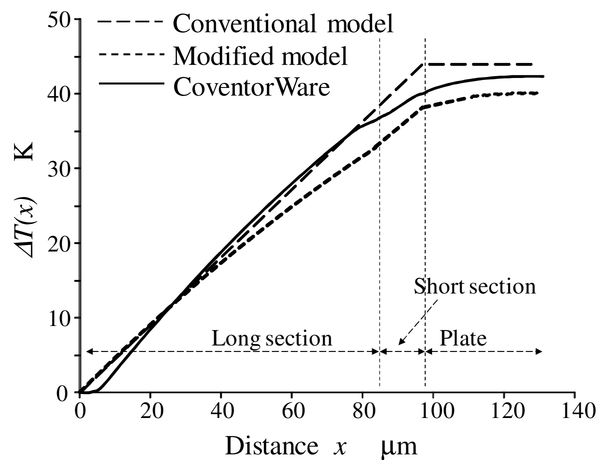

(a) (b)

Figure 8. (a) CoventorWare 3-D thermal profile, and (b) CoventorWare and analytical 2-D thermal profiles under vacuum conditions for device FA1.

The average temperature along the length of the metal film resistor can be determined from figures 7 and 8, and with the known input thermal power, the theoretical thermal conductance for each device can be determined at atmospheric pressure and under vacuum conditions.

From figure 7 it is evident that the inclusion of the sidewall effect F_{sw}, the characteristic thermal length L_{th} and the constriction resistance R_C, greatly improved the accuracy of the analytical modelling of the device. The fact that the CoventorWare simulation result has a slightly lower average temperature than the modified analytical model, indicates that the sidewall effect may be slightly underestimated in our model. This lower average temperature of the CoventorWare simulation may, however, also be due to the slow increase in temperature with distance where the supporting leg connects with the substrate ($x = 0$) which we do not model analytically. It is furthermore interesting to note that the sidewall effect of

gaseous conduction can be observed in the atmospheric pressure case in figure 7(a) where the edges of the plate are cooler than the rest of the plate.

In figure 8 are shown similar results for the FA1 test device under vacuum. In this case both the modified model and conventional model are fairly close to the simulated CoventorWare values.

6. Parameter extraction

A thin film metal resistor value as a result of a temperature increase can be modelled as

$$R_B(\overline{\Delta T}) = R_O(1+\alpha\times\overline{\Delta T})$$

with $\overline{\Delta T}$ = the average temperature along the length of the resistor. In our devices the temperature will not be constant along the length of the thin film resistor. The TCR of the Ti metal layer was experimentally determined as α = 0.104 %/K, following the above linear relationship closely.

By passing a bias current I_B through the bolometer, and measuring the bolometer resistance R_B as a function of bias current, the thermal conductance can be determined. Using the above equation of resistance as a function of temperature change, as well as the fact that

$$\overline{\Delta T} = \frac{P}{G} = \frac{I_B^2 R_B}{G} \qquad {}^{\circ}C$$

it can be shown that

$$\frac{1}{R_B} = \frac{1}{R_{BO}} - \frac{\alpha I_B^2}{G}$$

By plotting the inverse of the bolometer resistance as a function of the bolometer bias current squared, the thermal conductance G can be determined from the slope of the graph. The experimental results for FA1 and FA2 under atmospheric pressure are given in figure 9. Unfortunately test devices packaged in a vacuum less than 0.1 mbar are not yet available.

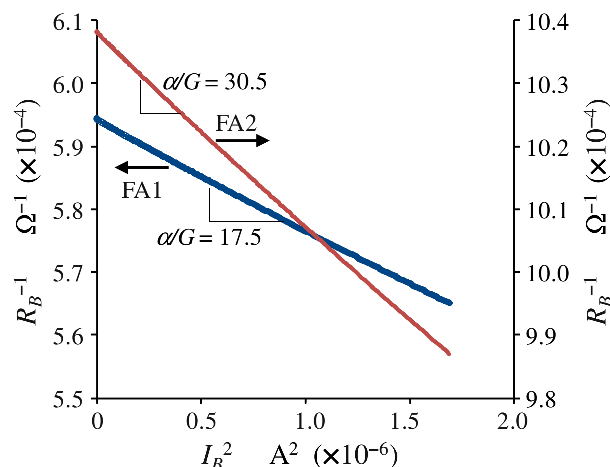

Figure 9. Experimental determination of thermal conductance at atmospheric pressure,

With the known values of the TCR (α), the experimental thermal conductance under atmospheric pressure can be determined from figure 9. The experimental values and the simulated values using CoventorWare under atmospheric pressure conditions are listed in table 3.

Table 3. Simulated and experimental thermal conductances under atmospheric pressure

Device	Atmospheric pressure: CoventorWare simulation G µW/K	Atmospheric pressure: Experimental extraction G µW/K	Vacuum: CoventorWare simulation G µW/K
FA1	72.4	59.4	0.6
FA2	44.7	34.1	1.2

In general the simulated values are higher than the experimental values. Since the gaseous thermal conductance at atmospheric pressure scales linearly with detector area and inversely with the plate to substrate cavity spacing d_s, the difference between the simulated and experimental thermal conductance will be as a result of variations in cavity separation due to stresses in the suspended plate and supporting legs. The simulated values were simulated with theoretical value $d_s = 2$ µm, and the experimental devices will have a different separation.

To experimentally determine the thermal capacitance H and thermal time constant τ, a transient measurement was performed. In this measurement the bolometer bias current i_B is switched between two values, I_L and I_H as shown in figure 10.

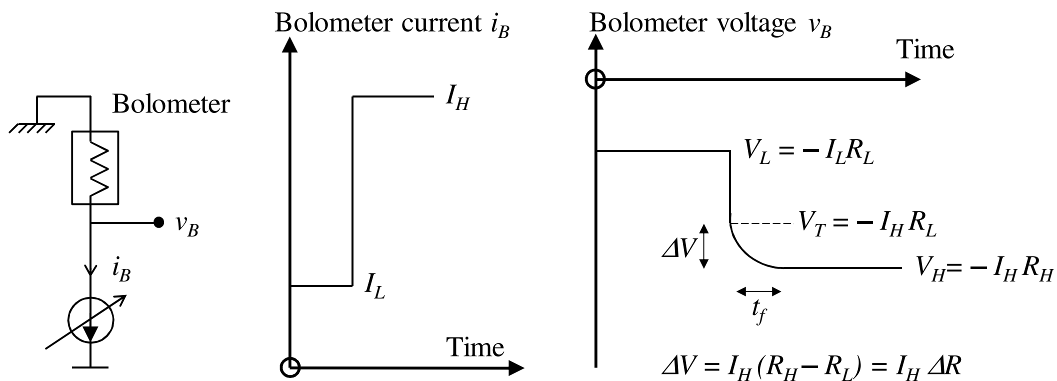

Figure 10. Transient switching behaviour of bolometer test circuit.

The bolometer steady state output voltage will change from V_L to V_H with $R_H > R_L$ the two steady state bolometer resistances. The transient behaviour between the two steady state values will be determined by the thermal transient characteristics of the bolometer. A typical result is shown in figure 11 for device FA1 under atmospheric pressure conditions. From the transient, the thermal time constant can be determined. The experimental time constant τ under atmospheric pressure for the test devices are shown in table 4, as well as the derived thermal capacitance H for each device. The atmospheric pressure thermal conductance and thermal capacity both scale linearly with the detector area and thus the two test devices will have the same atmospheric pressure thermal time constant.

Table 4. Experimental atmospheric pressure thermal time constant and thermal capacity

Device	Thermal time constant τ µs	Thermal capacity H nJ/K
FA1	160	9.5
FA2	164	5.6

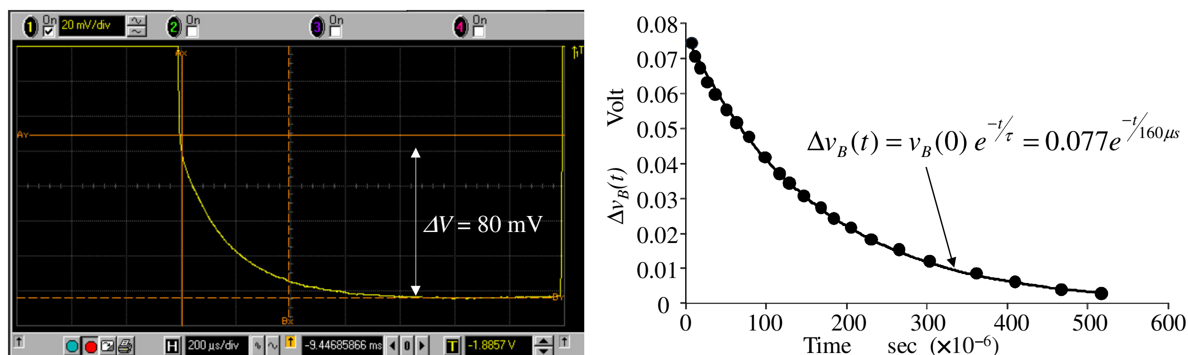

Figure 11. Experimental switching transient and exponential time constant fit.

7. Conclusion

A modified theoretical model has been proposed for microbolometers. It was shown that this model approximates the CoventorWare simulation quite well, especially for devices under atmospheric pressure. Extracted experimental values of the thermal parameters were compared to the theoretical values and differences explained.

8. Acknowledgement

This project was financially sponsored by the AMTS (Advanced Manufacturing Technology Strategy), a strategy of the Department of Science and Technology.

9. References

1. P.W. Kruse and D.D. Skatrud (Editors), "Uncooled infrared imaging arrays and systems", Semiconductors and Semimetals, Volume 47, 1997, Academic Press, London, ISBN 0-12-752155-0.

2. H. Baltes, O. Paul and O. Brand, "Micromachined thermally based CMOS microsensors", Proceedings of the IEEE, Vol. 86, No. 8, August 1998, pages 1660 to 1676.

3. A. Rogalski, "Optical detectors for focal plane arrays", Opto-Electronics Review, Vol. 12, No. 2, 2004, pages 221 to 245.

4. P. Eriksson, J.Y. Andersson and G. Stemme, "Thermal characterization of surface-micromachined silicon nitride membranes for thermal infrared detectors", Journal of Microelectromechanical systems, Vol. 6, No. 1, March 1997, pages 55 to 61.

5. N. Topaloglu, P.M. Nieva, M. Yavuz, J.P. Huissoon, "A novel method for estimating the thermal conductance of uncooled microbolometer pixels", Proceedings of the IEEE International Symposium on Industrial Electronics ISIE 2007, 4-7 June 2007, Vigo, Spain, pages 1554 to 1558.

6. N. Topaloglu, P.M. Nieva, M. Yavuz, J.P. Huissoon, "Modeling of thermal conductance in an uncooled microbolometer pixel", Sensors and Actuators A, Vol. 157, 2010, pages 235 to 245.